Solution-processed, high-performance n-channel organic microwire transistors

Joon Hak Oh[a], Hang Woo Lee[a], Stefan Mannsfeld[a], Randall M. Stoltenberg[b], Eric Jung[a], Yong Wan Jin[c], Jong Min Kim[c], Ji-Beom Yoo[d], and Zhenan Bao[a,1]

Departments of [a]Chemical Engineering and [b]Chemistry, Stanford University, Stanford, CA 94305; [c]Samsung Advanced Institute of Technology, Giheung-gu, Yongin-si, Gyunggi-do 449-712, Korea; and [d]School of Advanced Materials Science and Engineering, Sungkyunkwan University, 300, Chunchun-dong, Jangan-gu, Suwon 440-746, Korea

Edited by John Rogers, University of Illinois, and accepted by the Editorial Board February 11, 2009 (received for review November 23, 2008)

The development of solution-processable, high-performance n-channel organic semiconductors is crucial to realizing low-cost, all-organic complementary circuits. Single-crystalline organic semiconductor nano/microwires (NWs/MWs) have great potential as active materials in solution-formed high-performance transistors. However, the technology to integrate these elements into functional networks with controlled alignment and density lags far behind their inorganic counterparts. Here, we report a solution-processing approach to achieve high-performance air-stable n-channel organic transistors (the field-effect mobility (μ) up to 0.24 cm^2/Vs for MW networks) comprising high mobility, solution-synthesized single-crystalline organic semiconducting MWs (μ as high as 1.4 cm^2/Vs for individual MWs) and a filtration-and-transfer (FAT) alignment method. The FAT method enables facile control over both alignment and density of MWs. Our approach presents a route toward solution-processed, high-performance organic transistors and could be used for directed assembly of various functional organic and inorganic NWs/MWs.

organic semiconductors | single crystals | solution processing | alignment

Solution-processable, high-performance n-channel (electron-transporting) organic semiconductors are indispensable for cost-effective production of all-organic, flexible complementary logic elements (1–3). To date, however, very few solution-processable, air-stable organic n-channel semiconductors matching the performance of amorphous silicon (a-Si) ($\mu \geq 0.1$ cm^2/Vs) have been reported (4–8). Organic semiconductor nano/microwires (NWs/MWs) have recently emerged as promising building blocks for various electronic and optical applications such as light-emitting diodes (LEDs) (9), field-effect transistors (FETs) (10), photoswitches (11), vapor sensors (12), solar cells (13), nanoscale lasers (14), optical waveguides (15), and memory devices (16). These unique materials combine the high-performance of single-crystalline structures with solution-processability by dispersion (17, 18). Several *p*-channel (hole-transporting) organic wires prepared by solution-processing have exhibited $\mu > 0.1$ cm^2/Vs for single-wire transistors (19–22), whereas only a few solution-synthesized n-channel organic wires have been reported, typically with low performance ($\mu \approx 10^{-3} - 10^{-2}$ cm^2/Vs) (23, 24).

Despite the intrinsic high mobility of single-crystalline wires, precise wire placement and wire-to-wire performance variation, due to the difference in the contact quality at the wire/insulator and wire/electrode interfaces, substantially hinder successful device integration (10, 25). Therefore, the technology to achieve network films of organic MWs deposited from a dispersion with controlled alignment and density is acutely desired. The integration of inorganic and metallic wires into functional network films has been extensively explored by using a number of methods such as the flow cell method (26), electric field (27, 28), magnetic field (29), electrospinning (30), chemical and biological surface-directed patterning (31, 32), Langmuir–Blodgett technique (33, 34), transfer-printing (35, 36, 37), and the blown-bubble method (38). Compared with their inorganic counterparts, however, organic wires are typically mechanically less robust, electromagnetically less active, and broader in size distribution; hence, the aforementioned alignment techniques cannot easily be applied to them.

Here, we report an approach for solution fabrication of high-mobility, air-stable n-channel organic transistors from aligned, single-crystalline organic semiconducting MWs using *N*,*N*′-bis(2-phenylethyl)-perylene-3,4:9,10-tetracarboxylic diimide (BPE-PTCDI, Fig. 1*A Inset*). The single-crystalline BPE-PTCDI MWs exhibited μ as high as 1.4 cm^2/Vs for the individual wire transistor, which is the highest reported for solution-processed n-channel organic semiconducting wire devices as well as an order of magnitude higher than the best performance (0.1 cm^2/Vs) of the vacuum-deposited thin-film transistors (TFTs) (39). Furthermore, we present a filtration-and-transfer (FAT) method that allows for efficient alignment of organic wires with controllable density as well as the formation of multiple, discrete MW patterns aligned in different directions. The FAT method produced highly aligned, densely packed MW networks with n-channel μ up to 0.24 cm^2/Vs and good current output uniformity. This work demonstrates a viable route toward solution-processed, high-mobility n-channel organic transistors, which are very rare, but essential for low-cost production of complementary circuits.

Results and Discussion

BPE-PTCDI molecules in a hot, concentrated solution readily self-assemble into wire forms upon cooling or addition of a nonsolvent. These wires usually adopt the bulk packing motif in which π-electron-rich aromatic planes are either stacked or slip-stacked. In such an arrangement, there is large anisotropy in the surface free energies leading to the formation of needle- or ribbon-shaped assemblies. In situ absorption spectral monitoring [see supporting information (SI) Fig. S1] showed that the absorption bands attributed to individual molecules (at 533, 494, 462, and 433 nm) decreased gradually with cooling time, whereas a new band corresponding to the crystalline phase appeared at a longer wavelength (≈665 nm). The self-assembled structures of BPE-PTCDI molecules can be assigned to the J-aggregates due to the red-shifted absorption band, similar to other perylene diimide derivatives (23, 40).

The diameter and the length of BPE-PTCDI wires could be tuned across a wide range by either the nonsolvent nucleation (seeded-growth) (18, 19) or solvent-exchange method (rapid solution dispersion) (18, 20, 23, 40) (see *Materials and Methods*). In the former, we controlled the nucleation density at the initial

Author contributions: J.H.O., H.W.L., Y.W.J., J.M.K., J.-B.Y., and Z.B. designed research; J.H.O., H.W.L., R.M.S., and E.J. performed research; J.H.O., H.W.L., S.M., and R.M.S. analyzed data; and J.H.O. and Z.B. wrote the paper.

The authors declare no conflict of interest.

This article is a PNAS Direct Submission. J.R. is a guest editor invited by the Editorial Board.

[1]To whom correspondence should be addressed. E-mail: zbao@stanford.edu.

This article contains supporting information online at www.pnas.org/cgi/content/full/0811923106/DCSupplemental.

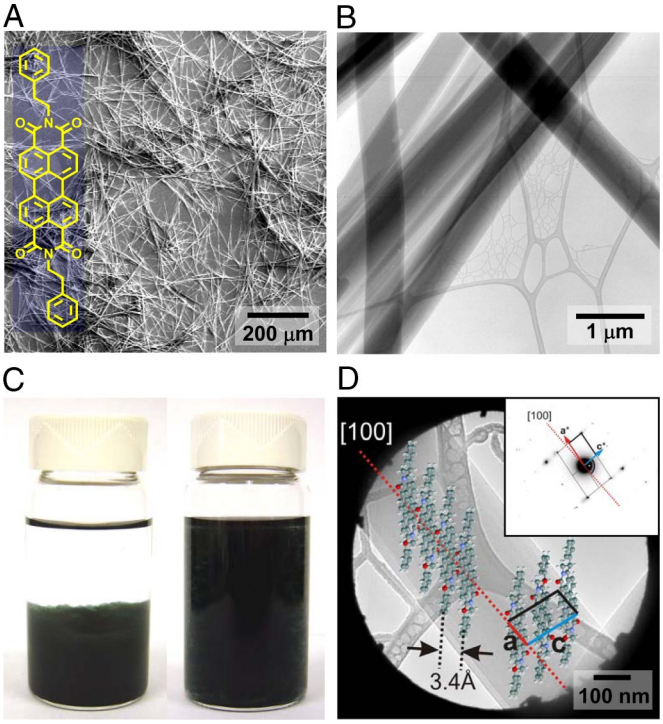

Fig. 1. Characterization of BPE-PTCDI MWs. (*A*) A SEM image of BPE-PTCDI MWs synthesized by the nonsolvent nucleation method. (*Inset*) The chemical structure of BPE-PTCDI. (*B*) A TEM image of BPE-PTCDI MWs. (*C*) Photographs displaying BPE-PTCDI MW dispersion in ethyl alcohol. (*D*) A TEM bright-field image with a selected area aperture of a single BPE-PTCDI MW. (*Inset*) the corresponding selected area electron diffraction (SAED) pattern and the molecular packing motif of a BPE-PTCDI MW, where BPE-PTCDI molecules have a slipped π-stacking structure along the long axis (the *a* axis) of the MW. The shortest vertical distance between the aromatic rings stacked along the *a* axis is 3.4 Å.

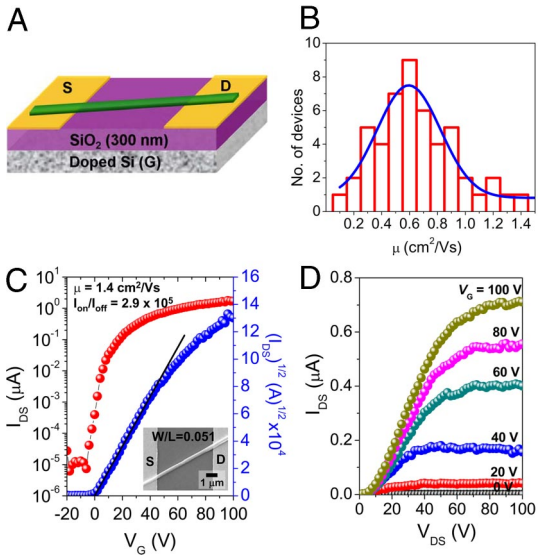

Fig. 2. BPE-PTCDI single-wire MW-TFT. (*A*) A single-wire MW-TFT structure, where S is the source, D the drain, and G the gate. (*B*) Histogram of field-effect mobility obtained from analysis of 50 randomly chosen devices measured under nitrogen atmosphere; the blue curve is a Gaussian fit giving an average mobility of 0.59 ± 0.23 cm^2/Vs. (*C* and *D*) I_{DS}-V_G characteristic recorded with V_{DS} = +100 V (*C*) and I_{DS}-V_{DS} characteristic with increasing V_G in steps of 20 V from 0 V to +100 V (*D*) for a BPE-PTCDI single MW-TFT device. (*C Inset*) A SEM image of the BPE-PTCDI single MW-TFT measured. The charge carrier mobility determined from the slope of the plot of $(I_{DS})^{1/2}$ vs. V_G was 1.4 cm^2/Vs.

stage of self-assembly by adding a small amount of a nonsolvent (typically <20 vol %), such as methanol, which leads to the immediate formation of nuclei for the crystal growth. The average diameter of wires decreased as the nucleation density increased (Fig. S2). In the solvent-exchange method, a small amount of concentrated solution was added to an excess of poor solvent, resulting in high nucleation density and narrow wire diameters down to several tens of nanometers. The length of the wires could be tuned from several millimeters to several tens of micrometers by controlling cooling speed and solvent mixing ratio. (Figs. S2 and S3).

For this work, BPE-PTCDI MWs synthesized by the nonsolvent nucleation method (Fig. 1 *A* and *B*, average diameter: 519 ± 194 nm and average length: 340 ± 68 μm) were used because they gave the best single-wire transistor performance. They could be easily dispersed in a poor solvent such as methyl alcohol or ethyl alcohol (Fig. 1*C*). The crystal structure and molecular packing of the BPE-PTCDI MWs were characterized with transmission electron microscopy (TEM). Several diffraction images taken at different locations of the same wire show the same diffraction pattern geometry, indicating the single-crystalline nature of the MWs. A typical bright-field (BF) image with the selected area aperture and the corresponding selected area electron diffraction (SAED) pattern from a BPE-PTCDI MW are shown in Fig. 1*D*. The diffraction patterns obtained on a single MW correspond to a single-crystalline phase with lattice constants of a = 8.7 Å, c = 4.7 Å, β = 79°, which is similar to the (010) plane of the bulk crystal (41). The shortest vertical distance between the aromatic ring systems of molecules along the *a*-axis is 3.4 Å. The orientation of the diffraction image indicates that the long MW axis is parallel to the crystallographic *a* axis, along which the BPE-PTCDI molecules exhibit a slipped π-stacking. It is well known that charge transport in aromatic molecular solids is more efficient along the direction in which the molecules exhibit π-stacking (17, 18, 42). Hence, in these wires, the most efficient direction of transport corresponds to the long axis of the MW.

BPE-PTCDI single MW-TFTs were fabricated in a bottom-gate bottom-contact configuration by drop-casting the MW dispersion in an ethyl alcohol solution (Fig. 2a). The active channel dimensions were estimated from the width (W) and length (L) of the MW crossing the source and drain electrodes. Fig. 2*B* represents the distribution of saturation regime charge carrier mobilities of 50 single MW-TFT devices tested under N_2 atmosphere. An average μ of 0.59 ± 0.23 cm^2/Vs, on-to-off current ratios (I_{on}/I_{off}) > 10^5 and threshold voltages (V_T) between −2 and +4 V were obtained. Single MW-TFTs normally exhibit a relatively wide range of electrical performance primarily because of the difference in contact quality of dielectric/semiconductor and electrode/semiconductor interfaces (10, 19, 25). Fig. 2 *C* and *D* displays the transfer and output characteristics for a single MW-TFT with the highest field-effect mobility (μ = 1.4 cm^2/Vs, I_{on}/I_{off} = 2.9 × 10^5, and V_T = +0.4 V). To the best of our knowledge, this is the highest mobility for n-channel transistors based on organic single crystal wires prepared by solution processing. It is comparable with the highest mobility of *p*-channel organic wires prepared by solution processing (20–22), as well as to the best performance of n-channel single-crystal organic transistors prepared with a free-space gate dielectric (43). Additionally, this mobility is approximately 10 times higher than that of vacuum-evaporated thin-film devices (0.1 cm^2/Vs) of the same molecules (39). The higher mobility of MW devices can be attributed to the high level of structural perfection of the single-crystal BPE-PTCDI MW and the fact that the π-stacking direction is parallel to the long axis of the MW. The nonlinear

onset of each output curve for MW-TFTs clearly shows signs of mild contact resistance (Fig. 2*D*). Nevertheless, the MW-TFT devices exhibit excellent gate modulation and current saturation. The mobility could likely be further increased by optimizing the contact behavior. MW-TFT devices measured under ambient condition after exposure to air for 1 h showed an average mobility of 0.38 ± 0.21 cm^2/Vs, $I_{on}/I_{off} > 10^5$, and V_T from +7 to +32 V. These MW-TFT devices remained stable (average μ of 0.32 cm^2/Vs) even after exposure to air for 54 days. The lowest unoccupied molecular orbital (LUMO) level of BPE-PTCDI MWs (−4.39 eV, Table S1) is lower than those of individual molecules (−4.10 eV) and vacuum-evaporated thin films (−4.26 eV) because of the enhanced electronic coupling between molecules in crystalline solids (42). The air-stability of BPE-PTCDI MW-TFTs is presumably due to the low LUMO level and the grain-boundary-free molecular packing that may act as a kinetic barrier to ambient oxidants (4–8).

Control over the alignment and density of organic semiconducting MWs is extremely important for practical applications, in that the current output of the transistor scales with the number of the MWs covering on the source-drain electrodes. Well-aligned, densely packed MWs allow the maximum number of MWs in contact with the electrodes and dielectric surface, resulting in the maximum current output and better performance uniformity.

To demonstrate high and uniform performance of aligned organic MWs, we designed a FAT alignment method, schematically illustrated in Fig. 3. BPE-PTCDI MWs were aligned by fluid flow through a mask in a modified, simple vacuum filtration setup. After filtration, the BPE-PTCDI MWs were located exclusively inside the open areas of a polydimethylsiloxane (PDMS) mask placed on a porous anodized aluminum oxide (AAO) membrane, producing patterned arrays of the MWs. The alignment of the MWs relative to the long axis of the stripe patterns improved significantly with increasing pressure difference across the filter stack. No mechanical fracture of the MWs was observed. The density of the aligned organic MWs inside the single pattern could be controlled easily by changing the concentration of the MW dispersion at a fixed loading volume into the filtration setup. The AAO membrane and PDMS mask containing the BPE-PTCDI MW patterns were then inverted on a substrate with a hydrophobic surface, such as a SiO_2 wafer treated with *n*-octadecyl triethoxysilane [$C_{18}H_{37}Si(OC_2H_5)_3$ (OTS)]. The hydrophobic BPE-PTCDI MWs were readily transferred from the hydrophilic surface of the AAO membrane to the OTS-treated SiO_2 substrate in water, presumably due to hydrophobic interactions between the MWs and OTS surface and surface energy difference between AAO membrane and OTS (37). Pulling the stacked layers out of deionized water resulted in a clean transfer of hydrophobic BPE-PTCDI MWs onto the hydrophobic OTS-treated SiO_2 surface. Filtration methods have been reported for the preparation of carbon nanotube (37, 44) and graphene (45) films. However, those methods only produced randomly oriented networks. Moreover, the membrane was either dissolved away (44), or a stamp was used to allow transfer of the film to the desirable support (37).

Fig. 4 *A* and *B* are typical optical microscopy images of aligned BPE-PTCDI MWs on AAO membrane after filtration. The majority of organic MWs are aligned along the long axis of the pattern. Fig. 4 *C* and *D* illustrates typical examples of BPE-PTCDI MWs transferred onto the OTS-treated SiO_2 substrate. The orientation of MWs is not altered by the transfer. It is noteworthy that high densities of aligned MWs (nearly complete coverage on desired pattern) can be achieved by simply increasing the concentration of the MW dispersion (Fig. 4*D*). The previously reported flow-assisted alignment method usually yields moderate densities of MW assemblies (26), and the microfluidic channels become clogged at a high density. Moreover, organic MWs with large diameters are mechanically less

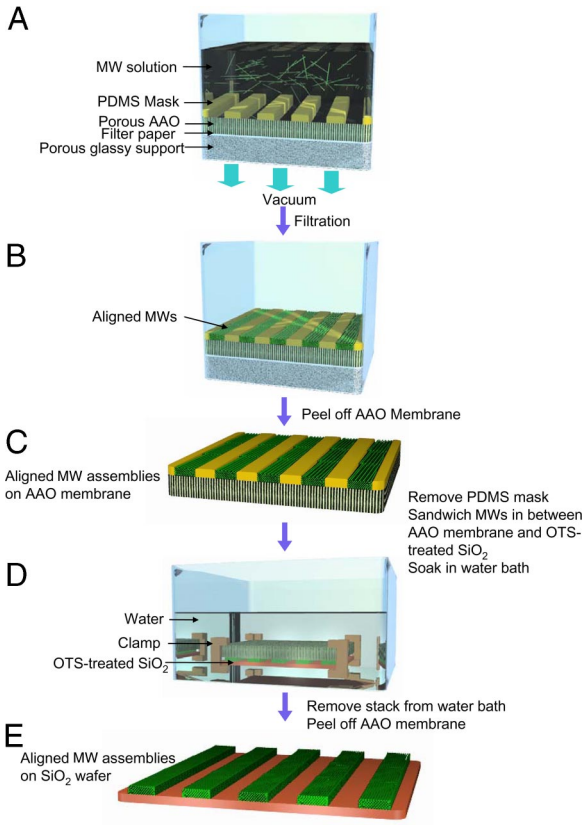

Fig. 3. Schematic diagram for FAT alignment of organic MWs. (*A*) FAT alignment apparatus loaded with the MW dispersion. A PDMS mask with open-stripe patterns is placed on a porous AAO membrane. The MW dispersion is filtered by applying vacuum. (*B*) MW assemblies reside exclusively inside the stripe patterns of the PDMS mask after filtration. The alignment of MWs along the stripe patterns is improved substantially as the pressure difference across the filter stack is increased. The density of the aligned MWs inside a single stripe pattern can be controlled by simply changing the concentration of the MW dispersion. (*C*) AAO membrane covered with patterned MWs inside the PDMS mask. (*D*) Illustration for the transfer of the aligned MW patterns from an AAO membrane to a desired wafer substrate in aqueous medium. MWs selectively adhere to the OTS-treated SiO_2 as water diffuses through the pores of the AAO membrane. (*E*) Aligned MWs were transferred onto the wafer.

robust than inorganic or metallic MWs, and strong shear forces in the fluidic channel may damage the organic MWs. Our FAT method is able to produce dense films of aligned and undamaged organic semiconductor MWs, which are important for achieving a high and uniform on-current. Multiple patterns composed of aligned MWs over a large area were readily obtained in a few minutes after filtration, as shown in Fig. 4 *E* and *F*.

Additional experiments were performed to investigate the factors affecting the alignment of the MWs. We found that the degree of alignment can be controlled by the vacuum pressure and that the MW density depends on the initial solution concentration. The MW angular distribution becomes substantially narrower as the vacuum pressure decreases, i.e., by increasing the filtration suction strength (Fig. 4g). As the base pressure decreased from the lowest filtration strength, 21 torr, to the highest, 10^{-4} torr, the average angular spread in a strip pattern with dimensions 200 μm × 4 mm dropped significantly from ±31° to ±7° with >85% of the organic MWs aligned in the intended direction (Fig. 4*G Inset*). The enhanced alignment is attributed to the increased fluid velocity through the PDMS mask with increased pressure difference across the filter stack. The increased velocity directs MWs falling to the AAO surface to lie

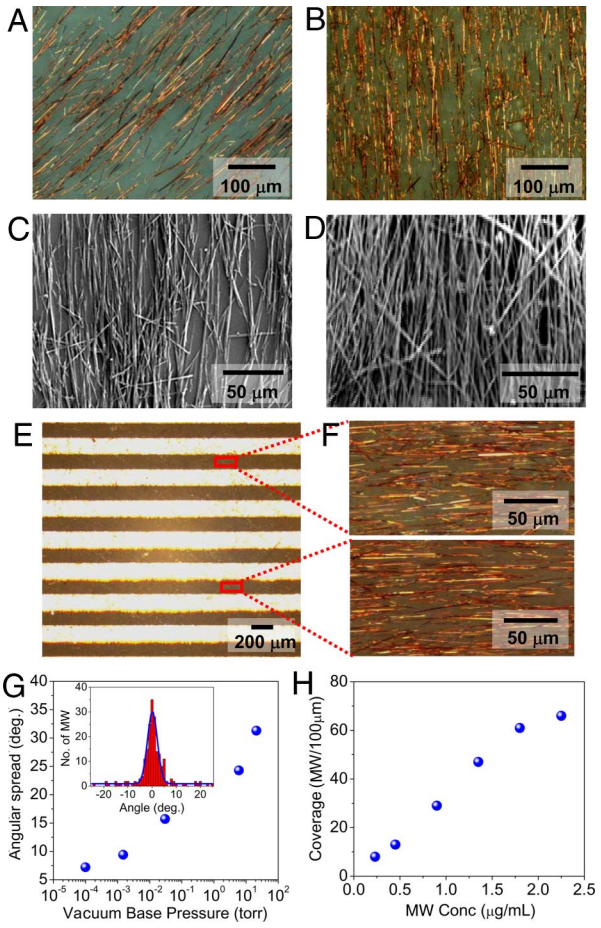

Fig. 4. Alignment and density control of BPE-PTCDI MWs. (*A* and *B*) Bright-field optical images of MW arrays on an AAO membrane after filtration (vacuum pressure 10^{-4} torr) from different concentrations of MW dispersion: 0.45 μg/mL (*A*) and 0.9 μg/mL (*B*) at a constant loading amount (5 mL). (*C* and *D*) SEM images of MW arrays transferred onto a wafer. The original MW dispersion had a concentration of 0.9 μg/mL (*C*) or 1.8 μg/mL (*D*). The vacuum pressure was kept at 10^{-4} torr. (*E*) Bright-field optical image of aligned MWs on an AAO membrane. (*F*) Zoom-in optical images of MWs in 2 different regions. (*G*) MW angular spread with respect to the stripe pattern direction versus vacuum pressure. Each data point was obtained by statistical analysis of angular distribution of ≈200 MWs (e.g., see *Inset*). (*Inset*) A histogram of MW angular distribution after filtration with a vacuum pressure of 10^{-4} torr; the blue curve is the Gaussian fitting giving an average angle of 0.1 ± 2.0 degrees with regard to the longitudinal direction of the pattern. The concentration of MW dispersion was 1.4 μg/mL. (*H*) Coverage of MWs versus MW dispersion concentration at a constant vacuum pressure of 10^{-4} torr. The average density was evaluated by counting the average number of MWs at any cross-section of the stripe pattern in the range of 100 μm.

parallel to the long axis of the pattern. Moreover, as the ratio of MW length to the open area width increases at a fixed filtration strength, the MW angular distribution also narrows, due to the relative enhancement in the torque (Fig. S4). A similar trend has been observed with other methods that rely on surface energy patterns to align MWs (46). MW surface density increased gradually with dispersion concentration (the average density changed from 8 MWs to 61 MWs per 100 μm by increasing the dispersion concentration from 0.23 μg/mL to 1.8 μg/mL) at a constant loading volume (5 mL) of MW dispersion and then approached a nearly constant value, which arose from the formation of multilayer stacks of the MWs over a critical concentration (Fig. 4*H*).

Unlike most other assembly methods, our alignment method can achieve multiple MW patterns aligned in different directions on the same substrate in 1 filtration step by using an appropriate mask. For example, we could form perpendicularly aligned, discrete MW patterns on the same substrate by using a mask with T-shaped pattern (Fig. S5). In addition, organic MWs could be aligned over nearly the entire area of an AAO membrane with 2.5-cm diameter, with pattern dimensions of several millimeters × centimeter scale (Fig. S6). The pressure drop across the filter stack can be increased by pressing the MW dispersion with a syringe. In theory, this method can be scaled to a larger area by using a larger filtration setup, given that the pressure difference is large enough to maintain sufficient fluid velocity for alignment. Moreover, our preliminary results revealed that the transfer of aligned and controlled density organic MW patterns can be readily performed on flexible plastic substrates (Fig. S7).

We fabricated transistors composed of BPE-PTCDI MW networks (MWnt-TFTs) by FAT method. Aligned MWs were transferred to the channel area of bottom contact substrates, with the MW alignment direction parallel to the channel length (Fig. 5*A* and Fig. S8). The distribution of the field-effect mobility for 50 low-density MWnt-TFTs, prepared from a MW dispersion of 0.45 μg/mL under the vacuum pressure of 10^{-4} torr, is displayed in Fig. 5*B*. For the calculation of mobility, we determined the W/L ratios from the sum of W/L ratios of the individual BPE-PTCDI MWs. The devices showed an average μ of 0.24 ± 0.07 cm^2/Vs with I_{on}/I_{off} of 10^5 to 10^6 and V_T from −20 to +14 V under ambient condition. Furthermore, to achieve uniform and high on-current levels without correcting the W/L ratios, we prepared high-density MWnt-TFTs using a high-concentration dispersion (2.3 μg/mL) for the FAT alignment (Fig. 5*C Inset*). In this case, the entire transistor channel area was covered with MWs, and the MW W/L correction was not applied to the mobility calculation. Typical transfer and output characteristics of high-density MW-TFTs are represented in Fig. 5 *C* and *D*. The average μ along the aligned long axis of the MWs for 50 high-density MWnt-TFTs was 0.14 ± 0.04 cm^2/Vs in air (Fig. 5*E*), the highest μ being 0.24 cm^2/Vs. The I_{on}/I_{off} ratios were $>10^5$ and V_T ranged from −13 to +24 V. This mobility is among the highest reported for solution-processed air-stable n-channel TFTs (4–8, 47). Our approach, comprising the simple, scalable synthesis of single-crystalline MWs and the straightforward transfer of the aligned MWs into active channel area, is of particular importance, in that the solution-processed TFTs exhibited mobilities surpassing the best performance of the vacuum-evaporated devices and that solution-deposited, high-mobility n-channel transistors are very rare. Moreover, the solvents (ethyl alcohol and water) used for MW dispersion and transfer are environmentally benign.

We also characterized the performance of MWnt-TFTs in which the MWs were either oriented perpendicular to the channel length or randomly oriented in the channel region. The mobility measured for MWs perpendicular to the channel length was ≈10^{-6} cm^2/Vs, whereas the randomly oriented networks yielded an average μ of 3.0×10^{-2} cm^2/Vs. These results clearly demonstrate that alignment of the MWs parallel to the channel length improves device performance significantly. The average μ for these high-density MWnt-TFTs is lower than that for single MW-TFTs because we did not correct for the channel width, and the MWs are not perfectly aligned, leaving gaps in the channel region. The curvature of MW surface can also reduce the effective contact with the dielectric and make the W/L ratio larger than the actual value, leading to an underestimated value for the mobility.

The uniformity of on-current is also important for various practical applications. The on-current (I_{DS} at V_G = +100 V and V_{DS} = +100 V) distribution of the high-density MWnt-TFTs measured from 50 devices (W = 270 μm and L = 100 μm) was found to be 11.3 ± 4.6 μA (Fig. 5*F*). These values compare favorably with the current-output distribution of previous Si NW-TFTs prepared by using the blown-bubble method, suggest-

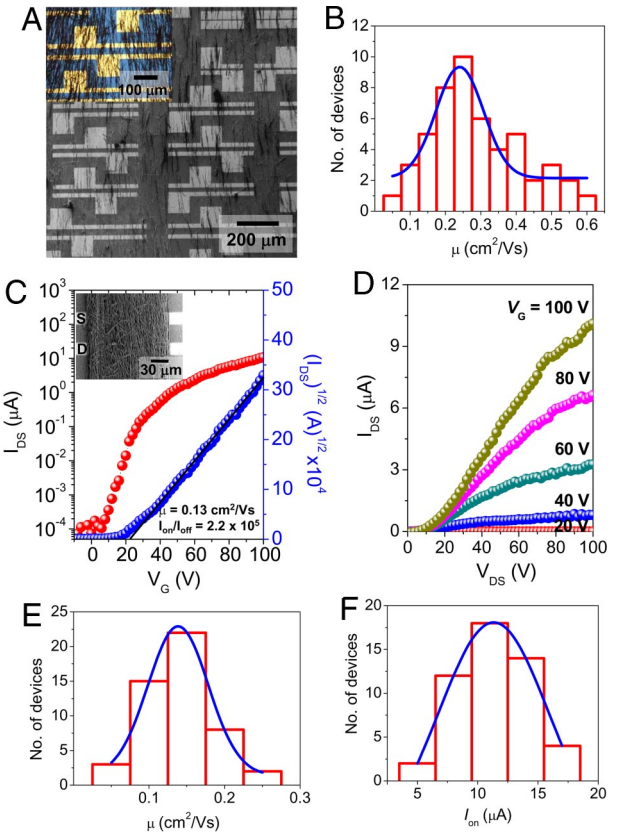

Fig. 5. TFT arrays composed of aligned BPE-PTCDI MWs as the active layer. (*A*) A SEM image of aligned MWs on a bottom-contact Si/SiO_2 substrate with the corresponding optical image (*Inset*). The concentration of MW dispersion and the vacuum pressure was 0.45 μg/mL and 10^{-4} torr, respectively. (*B*) Histogram of the field-effect mobility for 50 randomly chosen TFTs containing multiple MWs: The blue curve is a Gaussian fit giving an average mobility of 0.24 ± 0.07 cm^2/Vs. The measurements were carried out in air. The overall W/L was determined from the sum of each MW W/L obtained from the width of the MW and the length across the source-drain electrodes. (*C* and *D*) Typical I_{DS}-V_G characteristic for a MWnt-TFT device composed of a densely packed BPE-PTCDI MWs measured in air with $V_{DS} = +100$ V (*C*) and I_{DS}-V_{DS} characteristic with increasing V_G in steps of 20 V from 0 V to +100 V (*D*). The densely packed MWnt-TFT device was prepared with a loading concentration of 2.3 μg/mL at a vacuum pressure of 10^{-4} torr. *C Inset* is a SEM image of typical densely packed MWnt-TFT. The W/L ratio for the calculation of mobility was determined by simply measuring the length and width of the pattern. (*E*) Histogram of the field-effect mobility for 50 randomly chosen, densely packed MWnt-TFT arrays. The blue curve is a Gaussian fit giving an average mobility of 0.14 ± 0.04 cm^2/Vs. (*F*) Histogram of I_{on} from 50 randomly chosen MWnt-TFT devices; a Gaussian fit gives an average output current of 11.3 ± 4.6 μA at $V_G = +100$ V and $V_{DS} = +100$ V. Pattern width of the MWnt-TFT devices was 270 μm, and the channel length was 100 μm.

ing that our method is also promising for integrated systems (38). The BPE-PTCDI MW-TFTs exhibited only a small hysteresis and a stable I_{on}/I_{off} in N_2 atmosphere under repeated bias sweeps (see *SI Text* and Figs. S9 and S10). In ambient condition, the V_T and hysteresis increased due to charge trapping by ambient oxidants (Fig. S11). The ambient stability will likely be further improved by dielectric surface engineering (48, 49). In addition to high performance, our method provides a route for fabricating solution-processed devices from highly crystalline molecules with poor solubility as well as from those with high solubility in common organic solvents. Our method opens up a direction for the fabrication of high-performance organic electronic devices.

Conclusion

We have demonstrated an approach to achieve solution-processed, high-performance, air-stable n-channel organic transistors with mobility up to 0.24 cm^2/Vs, enabled by high-mobility single-crystalline n-channel organic MWs and an efficient, environmentally benign method for MW alignment and controlled density. Individual single-crystalline BPE-PTCDI MW-TFTs showed charge carrier mobilities up to 1.4 cm^2/Vs, which is the highest among the solution-processed n-channel organic semiconducting wire devices. The ability to align organic MWs with high density enables high uniform on-currents from MW-TFT devices. Our method allows for multiple, discrete MW patterns aligned in different directions on the same substrate at once, and it is also applicable to flexible substrates. The FAT alignment method opens up possibilities for using single-crystalline organic MWs for high-performance solution-processable transistors. It should also be potentially applicable to directed, hierarchical assemblies of various other functional organic and inorganic NWs/MWs.

Materials and Methods

Preparation of BPE-PTCDI MWs. BPE-PTCDI was purified 3 times by vacuum sublimation in a 3-temperature-zone furnace before use. BPE-PTCDI (18 mg) was dissolved in refluxing *o*-dichlorobenzene (15 mL) in a round-bottom flask with magnetic stirring. In the nonsolvent nucleation method, methyl alcohol (3 mL) was added into the solution and then stirred for 10 s. As the solution cooled, its color changed gradually from orange to dark green. After several hours, cotton-like BPE-PTCDI MWs were observed floating in the solution. The solution was vacuum-filtered with a porous anodized aluminum oxide (AAO). During the filtration, the BPE-PTCDI MWs were washed with an excess of ethyl alcohol, and redispersed in a vial containing ethyl alcohol.

FAT Alignment of MWs. A PDMS mask (≈5-μm thickness) with stripe patterns was prepared and placed on an AAO membrane with a pore diameter of 200 nm. This assembly was placed on a filter paper in a fritted glass funnel. A BPE-PTCDI MW dispersion was poured into the funnel while pulling vacuum. After the solvent was completely filtered away, BPE-PTCDI MWs were aligned in the stripe patterns of the PDMS mask. The AAO membrane supporting the patterned MWs was peeled off from the porous glassy support, and inverted onto an *n*-octadecyl triethoxysilane OTS-treated SiO_2/Si wafer, with MWs in contact with the OTS surface. The stacked layers were clamped together and moved into a bath of deionized water. After several minutes, the aligned BPE-PTCDI MWs were transferred from the hydrophilic AAO surface to the hydrophobic OTS-treated SiO_2/Si wafer. The clamps, PDMS mask and AAO membrane were removed, and the SiO_2/Si wafer containing highly aligned BPE-PTCDI MWs was thoroughly dried in a vacuum oven at 70 °C for 12 h.

Device Fabrication and Characterization. MW-TFTs were fabricated on a wafer with a thermally grown 300-nm-thick SiO_2 dielectric on highly doped n-type Si as a gate electrode. Bottom-contact devices (channel lengths 2, 5, 10, 20, 30, and 100 μm) were prepared by defining source-drain electrodes (metal thickness: Ti, 1.5 nm; Au, 40 nm) via conventional photolithography on top of SiO_2/Si wafers. To obtain better performance, the SiO_2/Si substrates were treated with OTS, as described previously (39). The capacitance (C_i) of the OTS-treated SiO_2 dielectric was 10 $nFcm^{-2}$ (see *SI Text* and Fig. S12). Various concentrations of BPE-PTCDI MW dispersions were used to fabricate MW-TFTs containing different densities of MWs (single MWs, multiple MWs, and MW bundles) in the channel area. The current-voltage (*I–V*) characteristics of the devices were measured by using a Keithley 4200-SCS semiconductor parameter analyzer. Key device parameters, such as charge carrier mobility (μ), on-to-off current ratio (I_{on}/I_{off}), and threshold voltage (V_T), were extracted from the drain-source current (I_{DS}) versus gate-source voltage (V_G) characteristics under the assumptions of conventional transistor equations (42): $I_{DS} = (WC_i\mu/2L)(V_G-V_T)^2$, where C_i is the capacitance per unit area of the gate dielectric layer, *W* and *L* are width and length of the channel region, respectively. The μ was determined in the saturation regime from the slope of plots of $(I_{DS})^{1/2}$ versus V_G.

ACKNOWLEDGMENTS. We thank Dr. Deuk Seok Chung for help in drawing 3D schematic diagrams of FAT alignment. J.H.O. acknowledges partial support from a Korea Research Foundation Grant (Ministry of Education and Human Resources Development KRF-2006-352-D00066). Z.B. acknowledges support from the National Science Foundation (NSF)–Division of Materials Research (DMR) solid-state chemistry under Award DMR-0705687, the Sloan Research Fellowship, Samsung Advanced Institute of Technology, and the Center for Polymeric Interfaces and Macromolecular Assemblies (NSF-Center Materials Research Science and Engineering Center under Award DMR-0213618).

1. Klauk H, Zschieschang U, Pflaum J, Halik M (2007) Ultralow-power organic complementary circuits. *Nature* 445:745–748.
2. Crone B, et al. (2000) Large-scale complementary integrated circuits based on organic transistors. *Nature* 403:521–523.
3. Allard S, et al. (2008) Organic semiconductors for solution-processable field-effect transistors (OFETs). *Angew Chem Int Ed* 47:4070–4098.
4. Usta H, Facchetti A, Marks T (2008) Air-stable, solution-processable n-channel and ambipolar semiconductors for thin-film transistors based on the indenofluorenebis-(dicyanovinylene) core. *J Am Chem Soc* 130:8580–8581.
5. Handa S, Miyazaki E, Takimiya K, Kunugi Y (2007) Solution-processible n-channel organic field-effect transistors based on dicyanomethylene-substituted terthienoquinoid derivative. *J Am Chem Soc* 129:11684–11685.
6. Babel A, Jenekhe SA (2003) High electron mobility in ladder polymer field-effect transistors. *J Am Chem Soc* 125:13656–13657.
7. Lee T-W, et al. (2005) All-solution-processed n-type organic transistors using a spinning metal process. *Adv Mater* 17:2180–2184.
8. Yan H, et al. (2009) A high-mobility electron-transporting polymer for printed transistors. *Nature* 10.1038/nature07727.
9. Niu Q, et al. (2008) Enhancing the performance of polymer light-emitting diodes by integrating self-assembled organic nanowires. *Adv Mater* 20:964–969.
10. Briseno AL, et al. (2008) Introducing organic nanowire transistors. *Mater Today* 11:38–47.
11. Tang Q, et al. (2007) Photoswitches and phototransistors from organic single-crystalline sub-micro/nanometer ribbons. *Adv Mater* 19:2624–2628.
12. Che Y, Yang X, Loser S, Zang L (2008) Expedient vapor probing of organic amines using fluorescent nanofibers fabricated from an n-type organic semiconductor. *Nano Lett* 8:2219–2223.
13. Xin H, Kim FS, Jenekhe SA (2008) Highly efficient solar cells based on poly(3-butylthiophene) nanowires. *J Am Chem Soc* 130:5424–5425.
14. O'Carroll D, Lieberwirth I, Redmond G (2007) Microcavity effects and optically pumped lasing in single conjugated polymer nanowires. *Nat Nanotechnol* 2:180–184.
15. Takazawa K, Kitahama Y, Kimura Y, Kido G (2005) Optical waveguide self-assembled from organic dye molecules in solution. *Nano Lett* 5:1293–1296.
16. Xiao K, et al. (2007) Single-crystal organic nanowires of copper-tetracyanoquinodimethane: Synthesis, patterning, characterization, and device applications. *Angew Chem Int Ed* 46:2650–2654.
17. Sundar VC, et al. (2004) Elastomeric transistor stamps: Reversible probing of charge transport in organic crystals. *Science* 303:1644–1646.
18. Zang L, Che Y, Moore JS (2008) One-dimensional self-assembly of planar π-conjugated molecules: Adaptable building blocks for organic nanodevices. *Acc Chem Res* 41:1596–1608.
19. Briseno AL, et al. (2007) Fabrication of field-effect transistors from hexathiapentacene single-crystal nanowires. *Nano Lett* 7:668–675.
20. Kim DH, et al. (2007) High-mobility organic transistors based on single-crystalline microribbons of triisopropylsilylethynyl pentacene via solution-phase self-assembly. *Adv Mater* 19:678–682.
21. Mas-Torrent M, et al. (2004) High mobility of dithiophene-tetrathiafulvalene single-crystal organic field effect transistors. *J Am Chem Soc* 126:984–985.
22. Mas-Torrent M, et al. (2004) Correlation between crystal structure and mobility in organic field-effect transistors based on single crystals of tetrathiafulvalene derivatives. *J Am Chem Soc* 126:8546–8553.
23. Briseno AL, et al. (2007) Perylenediimide nanowires and their use in fabricating field-effect transistors and complementary inverters. *Nano Lett* 7:2847–2853.
24. Briseno AL, et al. (2008) Self-assembly, molecular packing, and electron transport in n-type polymer semiconductor nanobelts. *Chem Mater* 20:4712–4719.
25. Xiao S, et al. (2006) Transferring self-assembled nanoscale cables into electronic devices. *J Am Chem Soc* 128:10700–10701.
26. Huang Y, Duan X, Wei Q, Lieber CM (2001) Directed assembly of one-dimensional nanostructures into functional networks. *Science* 291:630–633.
27. Zhang Y, et al. (2001) Electric-field-directed growth of aligned single-walled carbon nanotubes. *Appl Phys Lett* 79:3155–3157.
28. Smith PA, et al. (2000) Electric-field assisted assembly and alignment of metallic nanowires. *Appl Phys Lett* 77:1399–1401.
29. Tanase M, et al. (2001) Magnetic alignment of fluorescent nanowires. *Nano Lett* 1:155–158.
30. Gao J, et al. (2004) Large-scale fabrication of aligned single-walled carbon nanotube array and hierarchical single-walled carbon nanotube assembly. *J Am Chem Soc* 126:16698–16699.
31. Karen K, et al. (2003) DNA-templated carbon nanotube field-effect transistor. *Science* 302:1380–1382.
32. Lee M, et al. (2006) Linker-free directed assembly of high-performance integrated devices based on nanotubes and nanowires. *Nat Nanotechnol* 1:66–71.
33. Jin S, et al. (2004) Scalable interconnection and integration of nanowire devices without registration. *Nano Lett* 4:915–919.
34. Acharya S, et al. (2006) A semiconductor-nanowire assembly of ultrahigh junction density by the Langmuir–Blodgett technique. *Adv Mater* 18:210–213.
35. Fan Z, et al. (2008) Large-scale, heterogeneous integration of nanowire arrays for image sensor circuitry. *Proc Natl Acad Sci USA* 105:11066–11070.
36. Meitl MA, et al. (2004) Solution casting and transfer printing single-walled carbon nanotube films. *Nano Lett* 4:1643–1647.
37. Zhou Y, Hu L, Grüner G (2006) A method of printing carbon nanotube thin films. *Appl Phys Lett* 88:123109.
38. Yu G, Cao A, Lieber CM (2007) Large-area blown bubble films of aligned nanowires and carbon nanotubes. *Nat Nanotechnol* 2:372–377.
39. Ling M-M, et al. (2007) Air-stable n-channel organic semiconductors based on perylene diimide derivatives without strong electron withdrawing groups. *Adv Mater* 19:1123–1127.
40. Balakrishnan K, et al. (2005) Nanobelt self-assembly from an organic n-type semiconductor: Propoxyethyl-PTCDI. *J Am Chem Soc* 127:10496–10497.
41. Mizuguchi J (1998) *N,N′*-bis(2-phenethyl)perylene-3,4:9,10-bis(dicarboximide). *Acta Crystallogr C* 54:1479–1481.
42. Coropceanu V, et al. (2007) Charge transport in organic semiconductors. *Chem Rev* 107:926–952.
43. Menard E, et al. (2004) High-performance n- and p-type single-crystal organic transistors with free-space gate dielectrics. *Adv Mater* 16:2097–2101.
44. Wu Z, et al. (2004) Transparent, conductive carbon nanotube films. *Science* 305:1273–1276.
45. Li D, et al. (2008) Processable aqueous dispersions of graphene nanosheets. *Nat Nanotechnol* 3:101–105.
46. Liu S, Tok JB-H, Locklin J, Bao Z (2006) Assembly and alignment of metallic nanorods on surfaces with patterned wettability. *Small* 2:1448–1453.
47. Katz HE, et al. (2000) A soluble and air-stable organic semiconductor with high electron mobility. *Nature* 404:478–481.
48. Virkar A, et al. (2009) The role of OTS density on pentacene and C_{60} nucleation, thin film growth and transistor performance. *Adv Funct Mater*, in press.
49. Chua L-L, et al. (2005) General observation of n-type field-effect behaviour in organic semiconductors. *Nature* 434:194–199.